

PREDICTING FUTURE STATES WITH SPATIAL POINT PROCESSES IN SINGLE MOLECULE RESOLUTION SPATIAL TRANSCRIPTOMICS

Parisa Boodaghi Malidarreh^{*,1,4} Biraaj Rout^{*,1,4} Mohammad Sadegh Nasr^{*,1,4}
 Priyanshi Borad^{*,2,4} Jillur Rahman Saurav^{*,1,4} Jai Prakash Veerla^{1,4}
 Kelli Fenelon^{2,4} Theodora Koromila^{†,2,4} Jacob M. Lubert^{†,1,3,4}

¹ Department of Computer Science and Engineering, University of Texas at Arlington

² Department of Biology, University of Texas at Arlington

³ Department of Bioengineering, University of Texas at Arlington

⁴ Multi-Interprofessional Center for Health Informatics, University of Texas at Arlington

ABSTRACT

In this paper, we introduce a pipeline based on Random Forest Regression to predict the future distribution of cells that are expressed by the Sog-D gene (active cells) in both the Anterior to posterior (AP) and the Dorsal to Ventral (DV) axis of the *Drosophila* in embryogenesis process. This method provides insights about how cells and living organisms control gene expression in super resolution whole embryo spatial transcriptomics imaging at sub cellular, single molecule resolution. A Random Forest Regression model was used to predict the next stage active distribution based on the previous one. To achieve this goal, we leveraged temporally resolved, spatial point processes by including Ripley's K-function in conjunction with the cell's state in each stage of embryogenesis, and found average predictive accuracy of active cell distribution. This tool is analogous to RNA Velocity for spatially resolved developmental biology, from one data point we can predict future spatially resolved gene expression using features from the spatial point processes.

Index Terms— Random Forest, Regression, *Drosophila*, Sog-D, Ripley's K-function, transcriptomics, embryogenesis

1. INTRODUCTION

Recent technological advances have made it possible to capture high resolution images from embryogenesis process that help researchers to study gene expression patterns.[1, 2]. One of the major challenges of the modern genomics era is to better understand how gene expression is regulated to support spatiotemporal outputs that change over the course of development. The early *Drosophila* embryo has served as a paradigm for how enhancers control patterning and has

demonstrated that the patterning process is complex and dynamic. It is known that multiple, transiently acting enhancers act sequentially to support changing outputs of expression for some genes[2, 3, 4], whereas other genes are controlled by enhancers that act over a longer period and support changing spatial outputs over time. For example, expression of the gene short gastrulation (*sog*) is driven by at least two co-acting enhancers that support temporally dynamic expression. Live imaging experiments offer the capacity to analyze gene expression dynamics with increased temporal resolution and linear quantification. However, genetic and live imaging techniques have outpaced analysis techniques to harvest the bountiful information contained within real-time movies of transcriptional dynamics with modern methods confined to static parameter cell and transcript tracking methods [1, 5, 6]. To assess these mutant enhancer phenotypes systematically, we developed a quantitative approach to measure the spatiotemporal outputs of enhancer-driven MS2-yellow reporter constructs as captured by in vivo imaging to provide information about the timing, levels, and spatial domains of expression. Using transgenic fly lines, we conducted live imaging of the GFP signal associated with the MS2 stem-loop reporter sequence. This MS2 cassette contains 24 repeats of a DNA sequence that produces an RNA stem loop when transcribed. The stem-loop structure is specifically bound by the phage MS2 coat protein (MCP). MCP fused to GFP binds to MS2-containing transcripts (i.e., *sog*_Distal.MS2) producing a strong green signal within the nuclei of *Drosophila* embryos at sites of nascent transcript production. In this system, the nuclear GFP signal is only observed as a single dot for every nucleus corresponding to nascent transcription of the one copy of the MS2-containing reporter transgene site integrated into the genome. Furthermore, the nuclear periphery is marked by a fusion of RFP to nuclear pore protein (Nup-RFP) [7]. The imaging protocol was optimized to provide spatial information across the entire dorsal-ventral (DV) axis of embryos with the fastest temporal resolution that also retains

*Equal contribution.

†Responsible authors. Email: jacob.luber@uta.edu, theodora.koromila@uta.edu

embryo viability. In brief, embryos were imaged on Zeiss LSM 900 continuously over the course of 2hr at an interval of 30s per scan (twice as fast compared to previous studies). Importantly, this imaging protocol is not phototoxic to embryos. Because spatial outputs likely change in time across the embryo for many gene expression patterns, we developed an image processing approach to collect detailed information in both time and space by capturing one lateral half of the embryos. With this qualified imaging dataset, our goal was to predict the distribution of active cell in each stage of the embryo development. Several methods have been proposed for the efficient prediction of temporal variables. Authors in [8] proposed a novel concept called RNA velocity, which is defined as the time derivative of the gene expression. This concept allows for the estimation of the future state of individual cells in standard scRNA-seq protocols. In [9], authors proposed a method to capture spatial proteomics data to map cell states in order to predict cancer patient survival. They utilized the Ripley’s K-function for capturing spatial features which inspired us in our proposed pipeline. We developed a feature extraction method and analysis pipeline that can be used to predict the future distribution of cells in which the *Sog-D* gene is expressed.

2. METHODS

We generated super resolution live imaging data expressing *sog* gene (control) and *sog-D* gene (case) in early embryo of *Drosophila* (9 case, 4 control). We conduct pre-processing, feature extraction, training, and testing Fig.1. Both the training and testing phases incorporate identical pre-processing and feature extraction steps. The videos shows real time images from embryonic development, which were manually given stage development labels: NC 13 early, NC 13 late, NC 14 A, NC 14 B, NC 14 C, NC 14 D. In the pre-processing step, we used a generalist, deep learning-based segmentation method called Cellpose, which can precisely segment cells in each frame of the embryo development. Active cells were identified based on prevalence of green pixels indicative of gene expression within the cell, and the active mask underwent feature extraction. During this stage, the masked images underwent a gridding procedure with a predetermined size. Subsequently, the entire imaging dataset was transformed into a tabular format, taking into account the spatial information of each cell. We utilized four different metrics to capture both local and global features in a frame including m_1 , m_2 for both AP and DV axes, Ripley’s k-function, and n (total number of cells in each grid). Here, m_1 and m_2 denote the first and second moments, respectively, capturing the distribution of active cells at each stage. Furthermore, Ripley’s k-function was employed to analyze spatial correlation and quantify deviations from a random spatial distribution. Equation 1 illustrates the formula for calculating Ripley’s k-function. Where, A is the area under each window with

constant radius, n is the number of data points, d_{ij} is the distance between two points, and e_{ij} is an edge correction weight. Then, the tabular data went through two steps of averaging on each stage and time correcting. Since our goal is to predict the distribution of active cells in each stage and we have different number of frames for each stage, we averaged the whole feature values based on each stage. Also, to account for temporal alignment, we implemented a one-stage shift in features, where we utilized the features from the previous stage in prediction of the current stage. Following the completion of the feature extraction process, the dataset undergoes preparation for training a random forest regression model, a supervised learning algorithm. The outcome of this pipeline is the count of active cells within each grid at a given stage, determined by the features from the preceding stage. Subsequent to training the model, its performance is evaluated using test data. During testing, all pre-processing and feature extraction steps are replicated, and the pre-trained random forest regression model is employed to forecast the count of active cells for each grid across various stages.

$$\hat{K}_r = \frac{A}{n(n-1)} \sum_{i=1}^n \sum_{i=1, j \neq i}^n 1(d_{ij} \leq r) e_{ij} \quad (1)$$

3. EXPERIMENT AND RESULTS

3.1. Main study

As outlined in the methodology section, during the feature extraction phase, square grids were applied to images, and the number of active cells within each grid was predicted. The key challenge was selecting the optimal grid size to enhance performance on test data. Consequently, we replicated the entire process of pre-processing and feature extraction for four distinct grid sizes: 250, 125, 62.5, and 31.25 (where the grid size of ‘n’ indicates the division of the entire image into $n \times n$ squares). We used three different metrics to calculate the model performance on test data for different grid sizes which are rmse (root mean squared error), mae (mean absolute error), and Kullback-Leibler (KL) Divergence. Fig.2 shows the experiment for different grid sizes. Our analysis revealed the same increasing trend in both rmse and mae as the grid size increases from 31.25 to 250 which indicated that a smaller grid size corresponds to a lower error. KL Divergence, which we also utilized as a metric, measures how one probability distribution diverges from a second one. Thus, the smaller value for it shows that two distributions are closer to each other. We used this criterion to see how well the pipeline can capture the trends in the active cells distribution. The KL Divergence for these four different grid sizes showed the different trend. Increasing the grid size from 31.25 to 250 yielded a decrease in KL Divergence. We had two options, the first one was to select 31.25 based on the lower rmse and mae. However, the problem was the average size of the cell was approximately 36 so if we set the grid size to 31.25 we have just one cell

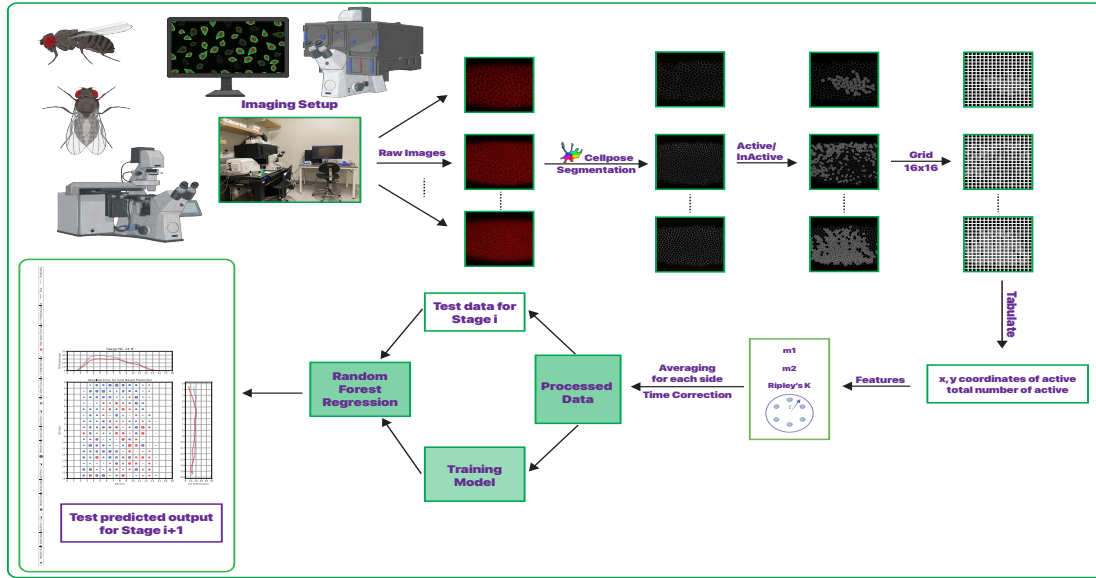


Fig. 1. Implemented pipeline, starting with the imaging process, followed by subsequent stages involving pre-processing, feature extracting, training, and testing. These steps collectively aim to predict the distribution of active cells for the next stage.

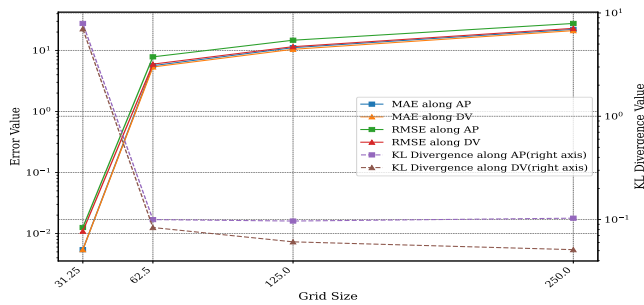


Fig. 2. The experiment for grid search to find the optimal grid size

in each grid which changes the problem to a classification of active or inactive for each grid which was not our purpose. Another option was to select the optimal grid size based on KL Divergence, which finally, We selected the grid size of 62.5 over 31.25. The decision of selecting 63.5 over 125.0 although the 125 had lower KL Divergence, is attributed to the computational constraints of calculating Ripley's k-function for larger grid sizes in our setup.

In subsequent experiment, we conducted an ablation study to discern the relative importance of features, identifying those deemed crucial for inclusion in the final release and those that may be omitted. Table 1 indicates the performance of different combinations of features. It can be concluded that features of the first row including Ripley's k-function and n are the most important features that we used them for training and testing the pipeline. All reported mae values underwent the K-fold cross validation method to mitigate the influence of random results.

To visualize the performance of the pipeline with selected features and parameters we tested the pre-trained model on test dataset. Fig 3 shows the distribution of active cell for the

Feature list	mae
n, Ripley's k-function	4.53
m2_DV, n, Ripley's k-function	4.73
m1_DV, n, Ripley's k-function	4.75
m1_DV, m2_AP, n, Ripley's k-function	4.77
m2_AP, n, Ripley's k-function	4.77

Table 1. The average mae value on K-fold cross validation over test dataset for different combinations of features for ablation study.

best, median and the worst prediction based on the average mae values.

3.2. Case and control study

As, we had 4 videos for case (transgenic) and 9 for control, we randomly selected 3 videos from each group for training and 1 for testing. Then, we averaged the AP_mae, DV_mae, and mean_mae for whole case and control experiments and calculated the difference between case and control for each of these metrics and the results were 1.86, -0.689, and 0.58 respectively. We also utilized cross-validation to avoid overfitting. These results show there is a difference between the performance of our pipeline on case and control in AP_mean and mean_mae. In other words, our method works better in predicting along AP axis and the mean of AP and DV on control data in comparison with the case one. However, the negative difference between case and control for DV_mae indicates that the pipeline works better in predicting the distribution on DV axis of case compared to control. In order to substantiate this assertion, we conducted two additional experiments: First, we leveraged Mixed-Effects modelling, which can account for both fixed effects (like the group:

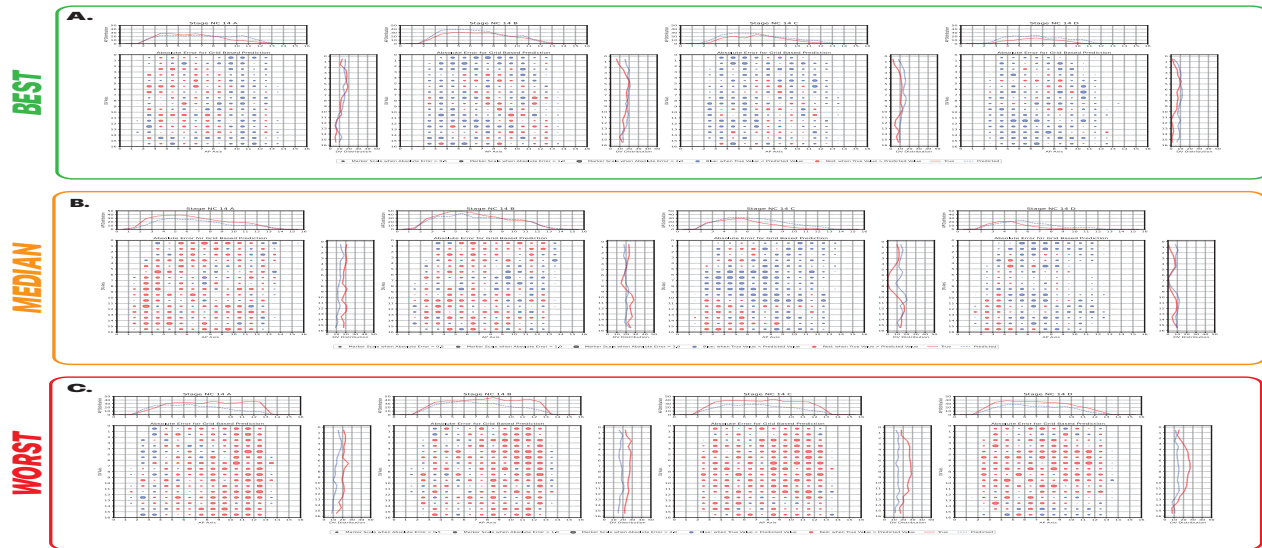


Fig. 3. The distribution of active cell for the best (A), median (B), and worst (C) accuracy based on mae values. For each A, B, and C from left to right stages are NC 14 A-D. For each stage the top and right plot shows the distribution of active cells along AP and DV axis respectively. The middle plot shows the absolute error in each grid.

case or control) and random effects (like the variation within videos and stages). The mixed-effects model can help in understanding the influence of these fixed and random effects on our dependent variables like DV_mae, AP_mae, mean_mae. The goal is to understand whether there is a significant difference in any metrics between the case and control groups, accounting for the variability introduced by different stages. The control group has, on average, a lower AP_mae compared to the case by about 1.828 units with the P-value of 0.003. It shows based on this test, there is a statistically significant difference in AP_mae between case and control groups. However, the result for DV_mae shows the control group has higher value by 0.714 units and 0.231 P-value. Also, the result for mean_mae indicates control has higher value by -0.557 units and 0.347 P-value. Two latter results for DV_mae and mean_mae cannot indicate any significant difference between case and control because of the high P-values. In addition, we implemented another empirical hypothesis testing called Bootstrap method. Bootstrap methods can be used to estimate the distribution of our metrics under the null hypothesis. To implement the bootstrap, we used the same metrics as previous method. we drew samples from the original dataset with replacement, to create a new dataset. Then, for each bootstrap sample, we computed the statistics of interest which are DV_mae, AP_mae, and mean_mae. By analyzing the this bootstrap distribution we can find the confidence intervals for each metrics. Fig 4 shows the Bootstrap distribution of mean difference in AP_mae, DV_mae, and mean_mae. It indicates that with 95% confidence interval the mean difference of AP_mae, (AP_mae(case) - AP_mae(control)) was between [0.69061964 3.11528348]. It can be concluded that with 95% confidence interval the AP_mae for case is

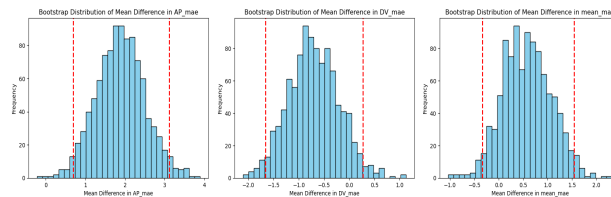


Fig. 4. The Bootstrap Distribution of Mean Difference in AP_mae, DV_mae, and mean_mae between case and control in 1000 iterations.

at least 0.69061964 units higher than case, which means the performance of the pipeline is better for control outperforms case one. These ranges for DV_mae and mean_mae are respectively, [-1.65878863 0.27041668] and [-0.33784703 1.5450897]. It can be seen that for DV_mae and mean_mae the ranges include zero means the performance of control can be better, equal, or worse than case. The results with Bootstrap method confirms the results derived from mixed effects method, which makes sense given that large amounts of training data are needed to model transgenic effects.

4. CONCLUSION

Our work presents several key contributions. Firstly, we have developed a novel and optimized imaging technology that delivers spatial information throughout the entire DV axis of an embryo. Secondly, we introduce an automated pipeline that effectively discriminates cell types with high accuracy. Lastly, our approach enables the accurate prediction of the stage-level distribution of active cells, based on data from the preceding stage.

5. COMPLIANCE WITH ETHICAL STANDARDS

All animal experiments were approved by the UTA IACUC review board. This study was performed in line with the principles of the Declaration of Helsinki. Approval was granted by the Ethics Committee of my institution.

6. ACKNOWLEDGMENTS

This work was supported by the Cancer Prevention and Research Institute of Texas (CPRIT) Recruitment of First-Time, Tenure-Track Faculty Members Grant (RR220015) (JML) and University of Texas System Rising STARS award (JML).

7. REFERENCES

- [1] Theodora Koromila and Angelike Stathopoulos, “Distinct roles of broadly expressed repressors support dynamic enhancer action and change in time,” *Cell reports*, vol. 28, no. 4, pp. 855–863, 2019.
- [2] Leslie Dunipace, Abbie Saunders, Hilary L Ashe, and Angelike Stathopoulos, “Autoregulatory feedback controls sequential action of cis-regulatory modules at the brinker locus,” *Developmental cell*, vol. 26, no. 5, pp. 536–543, 2013.
- [3] Hannah K Long, Sara L Prescott, and Joanna Wysocka, “Ever-changing landscapes: transcriptional enhancers in development and evolution,” *Cell*, vol. 167, no. 5, pp. 1170–1187, 2016.
- [4] Michael W Perry, Jacques P Bothma, Ryan D Luu, and Michael Levine, “Precision of hunchback expression in the drosophila embryo,” *Current biology*, vol. 22, no. 23, pp. 2247–2252, 2012.
- [5] Bomyi Lim, Tyler Heist, Michael Levine, and Takashi Fukaya, “Visualization of transvection in living drosophila embryos,” *Molecular cell*, vol. 70, no. 2, pp. 287–296, 2018.
- [6] Anthony Birnie, Audrey Plat, Cemil Korkmaz, and Jacques P Bothma, “Precisely timed regulation of enhancer activity defines the binary expression pattern of fushi tarazu in the drosophila embryo,” *Current Biology*, 2023.
- [7] Tanguy Lucas, Teresa Ferraro, Baptiste Roelens, Jose De Las Heras Chanes, Aleksandra M Walczak, Mathieu Coppey, and Nathalie Dostatni, “Live imaging of bicoid-dependent transcription in drosophila embryos,” *Current biology*, vol. 23, no. 21, pp. 2135–2139, 2013.
- [8] Gioele La Manno, Ruslan Soldatov, Amit Zeisel, Emelie Braun, Hannah Hochgerner, Viktor Petukhov, Katja Lidschreiber, Maria E Kastriiti, Peter Lönnerberg, Alessandro Furlan, et al., “Rna velocity of single cells,” *Nature*, vol. 560, no. 7719, pp. 494–498, 2018.
- [9] Monica T Dayao, Alexandro Trevino, Honesty Kim, Matthew Ruffalo, H Blaize D’Angio, Ryan Preska, Umamaheswar Duvvuri, Aaron T Mayer, and Ziv Bar-Joseph, “Deriving spatial features from in situ proteomics imaging to enhance cancer survival analysis,” *Bioinformatics*, vol. 39, no. Supplement_1, pp. i140–i148, 2023.